Supplemental Experimental Procedures

Section S.1: NO_x diagnostic: NDIR/UV

NDIR/NDUV stands for non-dispersive infra-red or ultra-violet absorption, because it does not contain dispersive optics often used in surveying the full absorption spectrum of gas samples. NDIR/UV uses gas specific light absorption, employing dedicated absorption cells (typically one per species) to discriminate and selectively measure the degree of light absorption as a direct measure of the species concentration [1]. For NO and N_2O we employed an IR radiation source (i.e., NDIR) while for NO_2 detection we used a UV source (i.e., NDUV) [2]. The detector consists of an opto-mechanical arrangement, which divides the gas sample between an absorption cell and a reference cell. Light absorption results in gas heating, which causes gas to outflow through a thin detection channel connecting the two chambers, and this is monitored by a micro-flow sensor providing the physical measurement [2]. A micro-mechanical chopper arrangement between the two cells periodically opens and closes. This increases sensitivity, enabling the background and absorption response to be clearly differentiated. The absolute flow, detected by the micro-flow sensor, is then used as measure of light absorption, which is directly correlated to a particular species concentration. We performed external calibration of the NDIR/UV using pre-mixed standards (Praxair Ltd.) for NO (0-20 % range) and NO_2 (0-10 % range), which are appropriately diluted to provide known concentrations across the sensor range.

Our modelling (see **section 3.2** in main paper) showed the discharge effluent to be dominated by NO and NO_2. N_2O was present as species in the model, but formed at negligible amounts. Experimentally, it was also monitored by a dedicated NDIR/UV channel. This species is indeed important to be monitored, due to its large global warming potential (GWP); however, no significant levels were detected (sensor range 0-20,000 ppm).

Section S.2: Quasi-1D chemical kinetics model

S.2.1 Dynamic gas velocity to translate the time-dependence of the balance equations into a spatial dependence, resulting in a quasi-1D model

Changes in species densities (i.e., equations 2-6 in main article) due to heat and stoichiometry changes of the N_2/O_2 conversion into NO_x are accounted for dynamically by taking account of the initial fixed mass flow rate Q_{inlet} with the assumption of isobaric conditions $p_0 \sim 1\ [atm]$. The velocity is given by:

$$v = \frac{Q_{inlet}}{\rho\, \pi\, r_{tube}^2}\ ,\ \rho = \sum_i m_i n_i\ \ ,\ \sum_i n_i = \frac{p_0}{k_B T_g} \tag{1}$$

Where Q_{inlet} is the fixed mass flow rate at the inlet, rho (i.e., $\rho(t)$) is the mass density for species with mass m_i and the total number density $\sum_i n_i\,(t)$ with (radially averaged) gas temperature $T_g(t)$.

In **figure SI.1** we plot the residence time [s] (x-axis) with the equivalent position [cm] (left y-axis) along with the associated dynamically calculated gas velocity [cm/s] (right y-axis) at (**a)** 10 L/min and (**b)** 20 L/min. The time and position intervals have a non-linear relationship given the dynamic gas velocity. As the gas transits the plasma region, heating causes it to accelerate considerably, resulting in a shorter residence time in the latter half of the plasma region. This is corroborated by the gas temperature profiles shown in **figure 5** in the main article, where the peak temperature is reached within the plasma region.

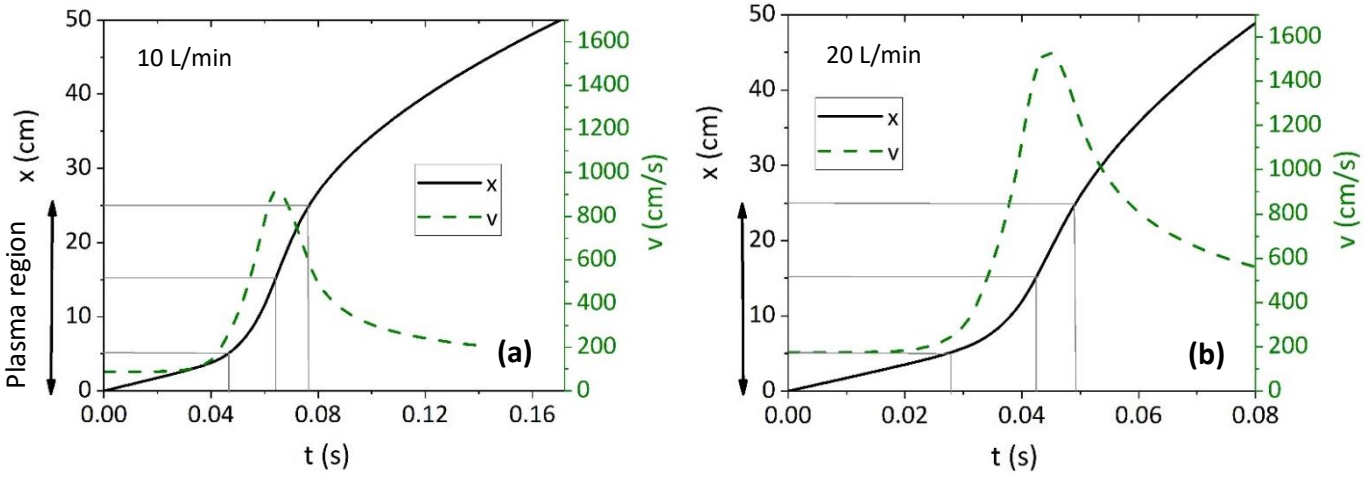

Figure SI.1: *Quasi-1D modelling results for 870 W power in the outer region of the plasma filament* ***3.5 < r₃ < 8 mm*** *(see below): residence time [s] (x-axis) with the equivalent position [cm] (left y-axis) along with the associated dynamically calculated gas velocity [cm/s] (right y-axis) at (**a)** 10 L/min and (**b)** 20 L/min.*

S.2.2 Power density as input in the model

The power density, used as input in the model, is adopted from the measured power and plasma volume. To determine the latter, the pixel intensity across radial cross sections of the plasma filament is extrapolated using camera images [3] and is found to have a Gaussian distribution. The normalised pixel intensity is fitted using a least square fitting with a Gaussian distribution (see equation 2 below) to determine the standard deviation (s) for each discharge condition. Indeed, estimation of the average power density is quite sensitive to calculation of the plasma volume and in particular to the plasma width or radius. The cylindrical plasma volume is given by $V_{plasma} = \pi {r_{plasma}}^2 l_{plasma}$. Small variations in the plasma radius, therefore, can represent relatively large changes in the power density due to the squared term in the plasma volume estimation. In this report, the plasma radius is found to increase with the applied power and is found to be less sensitive to changes in gas flow rate.

The full width at half maximum (FWHM) is often chosen as a representative width in many previous studies of this kind [4-7]. This, however, may lead to significant errors in capturing the average power density of the plasma. In order to alleviate this dependence and also to provide some spatial resolution to the modelling (in the radial direction) we solve for a collection of quasi-1D models, where each model derives its plasma volume (and hence power density) by choice of a plasma radius at the 'n^{th}' fraction of the light intensity maximum M (which occurs here at the centre of the quartz tube) derived from our Gaussian fitting of the light intensity across the plasma filament. The plasma radius at the full width n^{th} maximum M or "FWnM" is given as:

$$M/_n = M \exp\left(\frac{-\left(\frac{r_{plasma}}{2}\right)^2}{2\sigma^2}\right), \text{ where } r_{plasma} = \sqrt{2 * \ln(n)}\ \sigma \qquad (2)$$

Here the plasma radius r_{plasma} is determined by the choice of the n^{th} fraction of the maximum M and is parameterized only by the fitted standard deviation σ. This approach provides an avenue for improving upon an arbitrary choice of the plasma boundary and hence the power density (e.g., based on the FWHM, where $n = 2$ and $r_{plasma} \sim 2.35\sigma$ for estimation of the plasma width/radius).

We apply the model with three different power densities (shown in **figure SI.2**). This is carried out by calculating the plasma volume using different radii based on different positions where the peak light emission has dropped with a factor n. The resulting power densities are chosen to represent the inner and outer regions of the plasma filament and provide a proxy for the radial distribution in the power density which gas molecules feel as they transit the plasma region. For the inner region closest to the centre of the tube and plasma filament, we employed the full width at three quarters maximum (FW3Q) where $n = 1.33$ (i.e., $r_1 \sim 1.33\ \sigma$). We also choose for

an adjoining inner region, i.e., the FWHM, where $n = 2$ (i.e., r_2~ 2.35 σ). In the outer region (i.e., r > 2.35 σ) we chose the full width at quarter maximum (FWQM), where $n = 4$ (i.e., the light intensity is one quarter of its maximum M which occurs at the centre of the discharge tube) to represent the plasma extent. Note that here the remaining volume of the gas plug is typically larger than the plasma volume (i.e., inner radius of the tube is 8 mm) as the plasma edge or boundary is present at this location. For the conditions simulated in our paper, namely, 870 W at 10 L/min and 20 L/min in air, we found a standard deviation of $\sigma = 3\ mm$ from the Gaussian fitting of the pixel intensity using images extracted from inside the waveguide. This results in three radial intervals: $0 < r_1 < 2.3$ mm, $2.3 < r_2 < 3.5$ mm and $3.5 < r_3 < 8$ mm. The plasma volume (and power density) is calculated using r_1^{plasma}= 2.3 mm, r_2^{plasma}= 3.5 mm and r_3^{plasma}= 5 mm (i.e., FWQM). It must be noted that the outer region of the gas plug includes the edge of the plasma filament (e.g., see photo of plasma filament in **figure 8** inset in main article). The full width quarter maximum (FWQM) calculated here as r_3^{plasma}= 5 mm is employed in the outer region (i.e., $3.5 < r_3 < 8$ mm) to calculate the plasma density. We therefore account for a smaller plasma volume in this section rather using the inner radius of the quartz tube at 8 mm, which would overestimate the plasma radial extent (and hence power density). The choice of FWQM marks a median choice in the interval of the outer region (i.e., $3.5 < r_3 < 8$ mm), which captures the physical scenario of a smaller plasma volume located in a larger gas plug volume. This approximation is typically employed in models that choose the FWHM for the plasma boundary, which is typically significantly smaller than the quartz tube radius. In our scenario this is employed only for the outer region of the filament.

Solving for three power densities in this way allows each model to be combined as a weighted summation to generate an improved estimation of the total NO_x produced. This is achieved by considering the contribution to the tube cross section (i.e., radius of 8 mm and cross-sectional

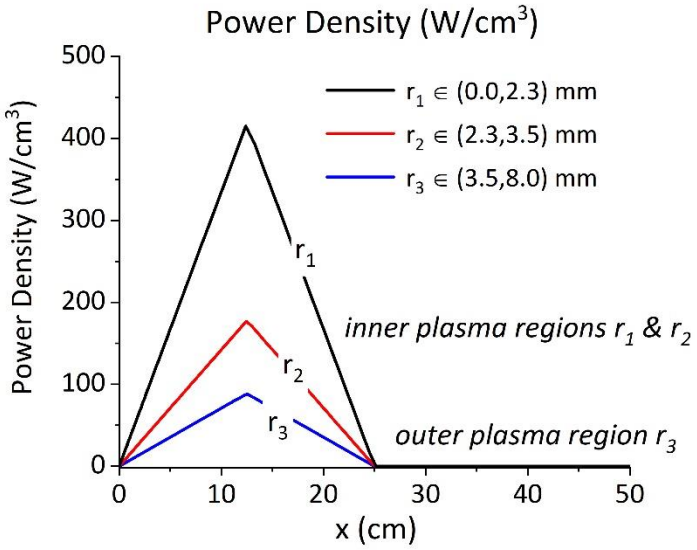

Figure SI.2: *Power density profiles used in our simulation of 870 W air MW plasma, in three regions: $0 < r_1 < 2.3$ mm, $2.3 < r_2 < 3.5$ mm and $3.5 < r_3 < 8$ mm, corresponding to two inner regions of the plasma filament and an outer region which contains the plasma edge.*

area of $\pi 8^2 \sim 201\ mm^2$) from each radial interval (i.e., 0 < r_1 < 2.3 mm, 2.3 < r_2 < 3.5 mm and 3.5 < r_3 < 8 mm). In our simulations, using a plasma length of 25 cm, the gas volume enclosed between the first inner region (i.e., 0 < r_1 < 2.3 mm) is equal to ~8% of the total gas plug volume; the volume enclosed in 2.3 < r_2 < 3.5 mm (i.e., the second inner region) is ~11 %; while the remaining cross-sectional contribution of the outer region of the gas plug (i.e., 3.5 < r_3 < 8 mm) is ~81% of the total gas plug cross-section (and hence volume). Note again here that the plasma radius in the outer region is selected to be smaller than the radius of the quartz tube to account for the plasma edge (i.e., which is approximated using the FWQM with r_3^{plasma}= 5 mm).

S.2.3 Nusselt number

The Nusselt number in the time-dependent gas thermal balance equation (equation 6 in the main paper) accounts for the heat loss to the boundaries. For Nu = 1, heat loss is purely conductive (i.e., diffusive) accounting for a stagnant situation. Values of Nu > 1 characterise enhanced thermal losses due to convective heat losses [8]. The Nusselt number can be expressed as $Nu = \frac{\alpha.(2*R)}{\lambda}$ where $\alpha\ [\frac{K}{cm^2\ s}]$ is the convective heat transfer coefficient (which encompasses both advective and diffusive heat transport), $\lambda\ [\frac{K}{cm\ s}]$ the thermal conductivity (i.e., diffusive heat transport) as mentioned above, and 2*R $[cm]$ the tube diameter as the representative length scale.

The power loss via heat transfer to the walls of a cylindrical discharge tube can be formulated [8] by dividing the heat flux deposited to the cylinder walls by the cylindrical plug volume with the formulation equivalently stated as $\frac{2\alpha}{R}(T_g - T_w) = Nu\frac{\lambda}{R^2}(T_g - T_w)$ [6,7]. In this work we chose a Nusselt number $Nu = 8$, which is in line with earlier reports in continuously powered discharges of this type where the choice coincides with assumption of a Parabolic distribution in radial temperature between a plasma filament and its boundary wall [4-7].

S.2.4 BOLSIG+

BOLSIG+ uses a two-term approximation to calculate the electron energy distribution function (EEDF). From the EEDF the mean electron energy and the different electron impact rate coefficients are obtained [9]. Super-elastic collisions for both vibrational and electronically excited states are included, as explained in our previous work [10,11]. The impact of vibrationally and electronically excited species on the EEDF is calculated explicitly using a detailed balancing based on the forward reaction cross section data. An explicit vibrational and electronic excitation scheme for N_2 and O_2 is therefore employed with regards to EEDF calculations in BOLSIG+ (i.e., no automatic inclusion of super-elastic collisions is enabled in lieu of the complete kinetics incorporated here). The EEDF is solved at each time step of the ZDPlasKin solution by calling BOLSIG+ to solve the stationary Boltzmann equation [9].

S.2.5 Chemistry

The full chemistry set used in our quasi-1D chemical kinetics model was recently developed and validated for a gliding arc plasmatron and rotating gliding arc plasma [4,5,12,13]. The chemistry set includes 97 different chemical species and the electron. These species react with each other in 1,214 electron impact reactions, 481 ionic reactions and 432 neutral reactions, as well as 2,478 vibration-vibration exchanges and vibration-translation relaxations between N_2 and O_2. The different species are detailed in **Table SI.1** below. Further details of the reaction rate coefficients and cross-section data employed can be found in our recent works [4,5,12,13].

Table SI.1: *Species included in our quasi-1D model for a N_2/O_2 mixture. $O_2(A_3C_3C_1)$ is a combination of three electronically excited states $O_2(A^3\Sigma)$, $O_2(C^3\Delta)$ and $O_2(c^1\Sigma)$ with a threshold energy of 4.5 eV.*

Neutral	**Excited**	**Charged**
O_2, O, O_3	$O_2(V_1 - V_{15})$, $O_2(A_1\Delta)$, $O_2(A_3C_3C_1)$ *, $O_2(B_1\Sigma)$, O(1D), O(1S)	e, O^+, O^-, O_2^-, O_2^+, O_4^-, O_4^+, O_3^-
N_2, N	$N_2(V_1 - V_{43})$, $N_2(^2D)$, $N_2(^3P)$, $N_2(A_1\Sigma)$, $N_2(A_3\Sigma)$, $N_2(B_3\Pi)$, $N_2(C_3\Pi)$	N_2^+, N_3^+, N_4^+
NO_2, NO, N_2O, N_2O_3, N_2O_4, N_2O_5		NO_2^+, NO_2^-, N_2O^-, N_2O^+, NO^+, NO^-, NO_3^-

S.2.6 Vibrational temperature

The vibrational temperatures $T_v^{(v=i\leftarrow v=j)}(K)$ are calculated based on the ratio of the j^{th} vibrational level to the i^{th} $(j > i)$ of the Boltzmann factor [14] between neighbouring vibrational number densities $n_{i,j}$ and the associated vibrational energy levels ($E_{i,j}$) of N_2 and O_2 :

$$T_v^{(v=i\leftarrow v=j)} = -\frac{E_j - E_i}{ln\,(\frac{n_j}{n_i})} \tag{3}$$

In this work, $T_v^{(v=i\leftarrow v=j)}(K)$ is calculated from the ratio of level 1 and 0 (ground state), i.e., $T_v^{(v=0\leftarrow v=1)}$.

Section S.3.1: Electronic image of experimental setup

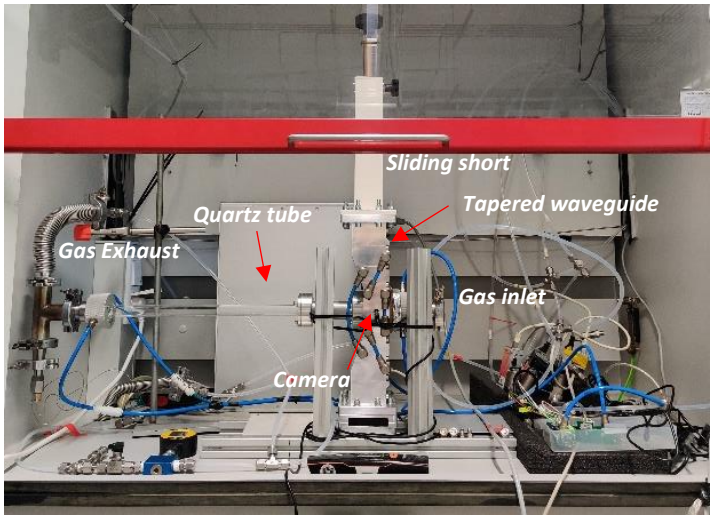

Figure SI.3: *Image of the plasma reactor at PLASMANT laboratories, UAntwerpen.*

A photo of the reactor is shown in **figure SI.3** above. Note the orientation of the plasma is horizontal. Gas inlet is located on the right-hand side with the gas exhausted at the left-hand side. The tapered section of MW waveguide (where ignition occurs) is located at the centre of the image with the power supply located below the fume hood (outside image). The NDIR/UV apparatus is located in the background near the exhaust line.

Section S.3.2: Monitoring exhaust temperature as a function of time

The temperature of the exhausted gas is measured (**figure SI.4**) to determine an approximate time interval for the reactor to reach steady state conditions from a room temperature start (i.e., reactor initially at room temperature). A thermocouple is placed in the stainless-steel exhaust tubing approximately 70 cm from the plasma ignition point downstream of the quartz discharge tube (~50 cm long). Data is fitted with an exponential function [15] using the temperature rise $\Delta T = T_f - T_i$ where T_i is the initial temperature (room temperature ~293 K) and T_f is the final or steady state temperature for a particular operating condition (i.e., power and flow conditions).

$$T(t) = T_i + \Delta T(1 - \mathrm{e}^{-\mathrm{t}/\tau}) \quad (4)$$

The time behaviour in equation (4) is described by a single parameter τ which is the (characteristic) time to reach ~63.2% or (1-1/e) fraction of ΔT. Fitting of thermocouple and model data based on equation (4) is carried out using an orthogonal distance regression (ODR) algorithm [16,17] for coefficient of determination $R^2 > 0.98$.

In **figure SI.4** we see a steady state is reached after ~800 seconds (~13.3 mins). The characteristic time derived from fitting with equation (4) above is determined as $\tau \sim 62$ s. The NO_x NDIR/UV measurements are performed at least 15 minutes after ignition once a thermal steady state is reached.

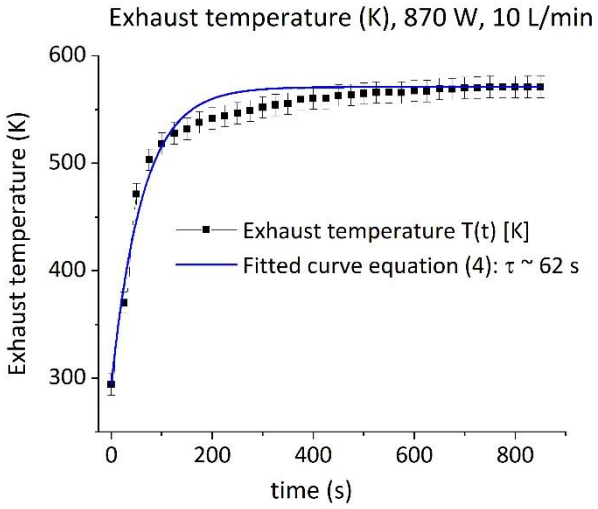

Figure SI.4: *Exhaust gas temperature time behaviour for 870 W air MW plasma, 10 L/min measured using a k-type thermocouple positioned downstream of the plasma region. Data is fitted with equation (4) giving a characteristic time of* $\tau \sim 62\ [s]$.

Section S.3.3: Total NO_x concentrations, including the individual values for NO and NO_2. The total NO_x and energy cost are also plotted in figure 1 in the main paper.

Table SI.2: *Measured NDIR/UV data used in* ***figure 1*** *in the main text.*

Power (W)	N_2/O_2 Mix (%)	Flow rate (L/min)	NO (%)	NO_2 (%)	Total NO_x (%)	Energy Cost (MJ/mol)	Total NO_x (L/min)	Energy Cost (MJ/L)
280	80/20	5	1.5	1.3	2.8	2.9	0.14	0.12
280	60/40	5	1.3	2.2	3.4	2.4	0.17	0.10
280	50/50	5	1.1	2.3	3.4	2.4	0.17	0.10
280	40/60	5	1.0	2.3	3.3	2.4	0.17	0.10
280	20/80	5	0.7	1.6	2.3	3.5	0.12	0.15
519	80/20	5	1.8	2.0	3.8	4.0	0.19	0.16
519	60/40	5	1.4	3.1	4.5	3.3	0.22	0.14
519	50/50	5	1.2	3.3	4.5	3.3	0.23	0.14
519	40/60	5	1.1	3.3	4.4	3.4	0.22	0.14
519	20/80	5	0.8	2.6	3.4	4.3	0.17	0.18
870	80/20	5	1.9	2.5	4.3	5.8	0.22	0.24
870	60/40	5	1.5	3.7	5.2	4.8	0.26	0.20
870	50/50	5	1.3	3.9	5.2	4.8	0.26	0.20
870	40/60	5	1.1	3.9	5.1	5.0	0.25	0.21
870	20/80	5	0.9	3.4	4.3	5.9	0.21	0.24
1072	80/20	5	1.8	2.7	4.5	6.9	0.22	0.29
1072	60/40	5	1.4	3.8	5.2	5.9	0.26	0.25
1072	50/50	5	1.3	4.0	5.2	5.9	0.26	0.25
1072	40/60	5	1.2	4.0	5.2	5.9	0.26	0.25
1072	20/80	5	1.1	4.0	5.0	6.1	0.25	0.26
280	80/20	10	0.9	0.4	1.3	3.1	0.13	0.13
280	60/40	10	0.9	0.8	1.6	2.5	0.16	0.10
280	50/50	10	0.8	0.9	1.7	2.4	0.17	0.10
280	40/60	10	0.7	0.9	1.6	2.5	0.16	0.10
280	20/80	10	0.5	0.6	1.2	3.5	0.12	0.15
519	80/20	10	1.5	1.1	2.6	2.9	0.26	0.12
519	60/40	10	1.3	2.0	3.3	2.3	0.33	0.10

519	50/50	10	1.2	2.2	3.3	2.3	0.33	0.09
519	40/60	10	1.0	2.2	3.2	2.3	0.32	0.10
519	20/80	10	0.8	1.7	2.5	3.0	0.25	0.13
870	80/20	10	1.9	1.8	3.7	3.3	0.37	0.14
870	60/40	10	1.5	3.1	4.6	2.7	0.46	0.11
870	50/50	10	1.3	3.2	4.6	2.7	0.46	0.11
870	40/60	10	1.2	3.2	4.4	2.8	0.44	0.12
870	20/80	10	0.9	2.4	3.3	3.7	0.33	0.15
1072	80/20	10	2.0	2.1	4.1	3.8	0.41	0.16
1072	60/40	10	1.5	3.4	5.0	3.1	0.50	0.13
1072	50/50	10	1.4	3.6	5.0	3.1	0.50	0.13
1072	40/60	10	1.2	3.6	4.8	3.3	0.48	0.14
1072	20/80	10	0.9	2.8	3.7	4.2	0.37	0.18
280	80/20	20	0.5	0.1	0.6	3.2	0.12	0.13
280	60/40	20	0.5	0.3	0.8	2.6	0.16	0.11
280	50/50	20	0.5	0.3	0.8	2.6	0.16	0.11
280	40/60	20	0.5	0.3	0.8	2.6	0.15	0.11
280	20/80	20	0.3	0.2	0.6	3.6	0.11	0.15
519	80/20	20	0.9	0.3	1.2	3.1	0.24	0.13
519	60/40	20	0.8	0.7	1.6	2.4	0.31	0.10
519	50/50	20	0.8	0.8	1.6	2.3	0.33	0.10
519	40/60	20	0.7	0.9	1.6	2.4	0.32	0.10
519	20/80	20	0.6	0.7	1.2	3.0	0.25	0.13
870	80/20	20	1.4	0.9	2.3	2.8	0.45	0.12
870	60/40	20	1.2	1.7	2.9	2.2	0.57	0.09
870	50/50	20	1.1	1.8	2.9	2.2	0.58	0.09
870	40/60	20	1.0	1.8	2.8	2.2	0.56	0.09
870	20/80	20	0.7	1.5	2.3	2.8	0.45	0.12
1072	80/20	20	1.6	1.3	3.0	2.6	0.59	0.11
1072	60/40	20	1.3	2.4	3.7	2.1	0.74	0.09
1072	50/50	20	1.2	2.7	3.8	2.0	0.77	0.08
1072	40/60	20	1.0	2.5	3.6	2.2	0.71	0.09
1072	20/80	20	0.8	1.9	2.8	2.8	0.55	0.12

Section S.3.4: Calculated vibrational distribution functions

In **figure SI.5** and **figure SI.6** we plot the calculated vibrational distribution function (VDF) (normalised to v=0) for $N_2(v)$ and $O_2(v)$ at various prominent positions throughout the plasma, along with the corresponding Boltzmann distributions, which represent the equivalent equilibrium vibrational distributions at these particular gas temperatures. The equivalent residence time for each position within the plasma is also shown for flow rates of 10 L/min and 20 L/min. For $N_2(v)$ we see a clear overpopulation of the VDF in the first part of the plasma (x = 5 cm), especially for 20 L/min (t_{res}=0.046 s), indicating a strong vibrational-translational (V-T) non-equilibrium, but at later positions (x = 15 cm) and at the end of the plasma (x = 25 cm) the VDF is not overpopulated with respect to the Boltzmann distribution (at both flow rates) with an equilibrium situation occurring between vibrational and translational temperatures. For $O_2(v)$, the VDF is overpopulated at x = 5 cm for 20 L/min (t_{res}=0.027 s) while for 10 L/min (t_{res}=0.046 s) a convergence of gas and vibrational temperatures is already present. Further into the plasma region (and at later residence times) this overpopulation at 20 L/min (i.e., x=15 cm, t_{res}=0.042) is significantly reduced, consistent with the equivalent residence time for 10 L/min (i.e., x=5 cm, t_{res} = 0.046).

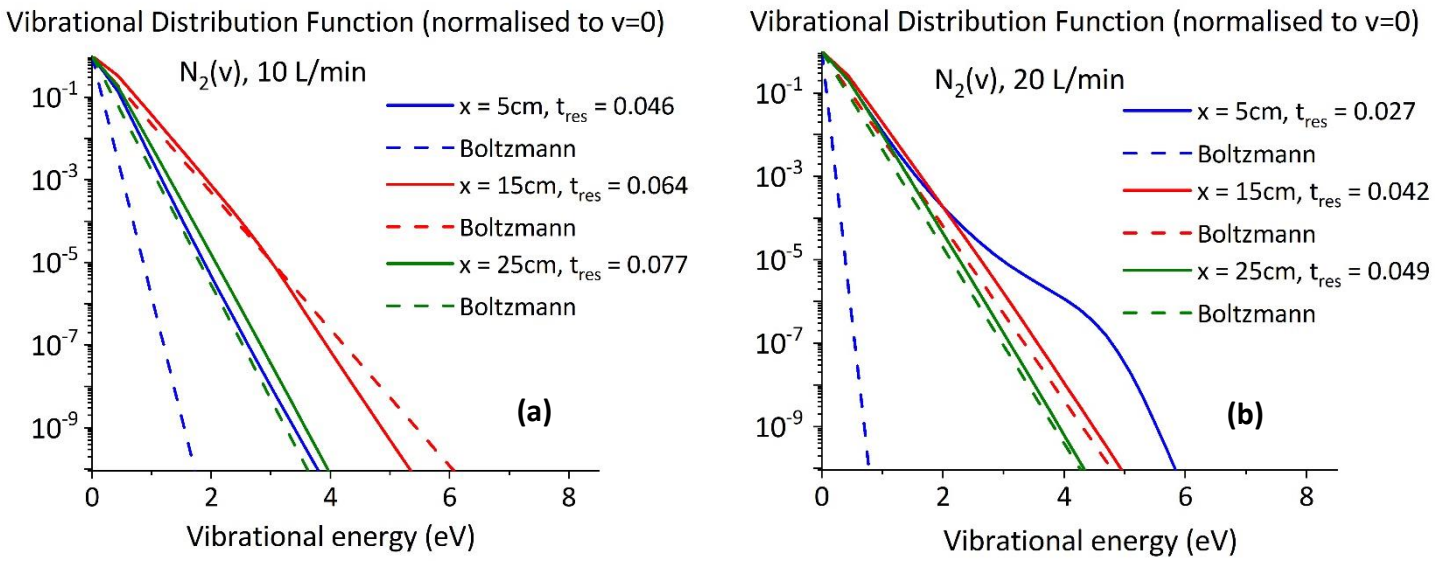

Figure SI.5: *Quasi-1D modelling results of the vibrational distribution of $N_2(v)$ levels for 870 W power,* ***3.5 < r_3 < 8 mm****, at* ***(a)*** *10 L/min and* ***(b)*** *20 L/min. The equivalent Boltzmann distribution is shown along with the VDF at three points inside the plasma region, namely, x=5 cm, x=15 cm and x=25 cm. The residence times up to each point in the discharge are also shown in the accompanying legend.*

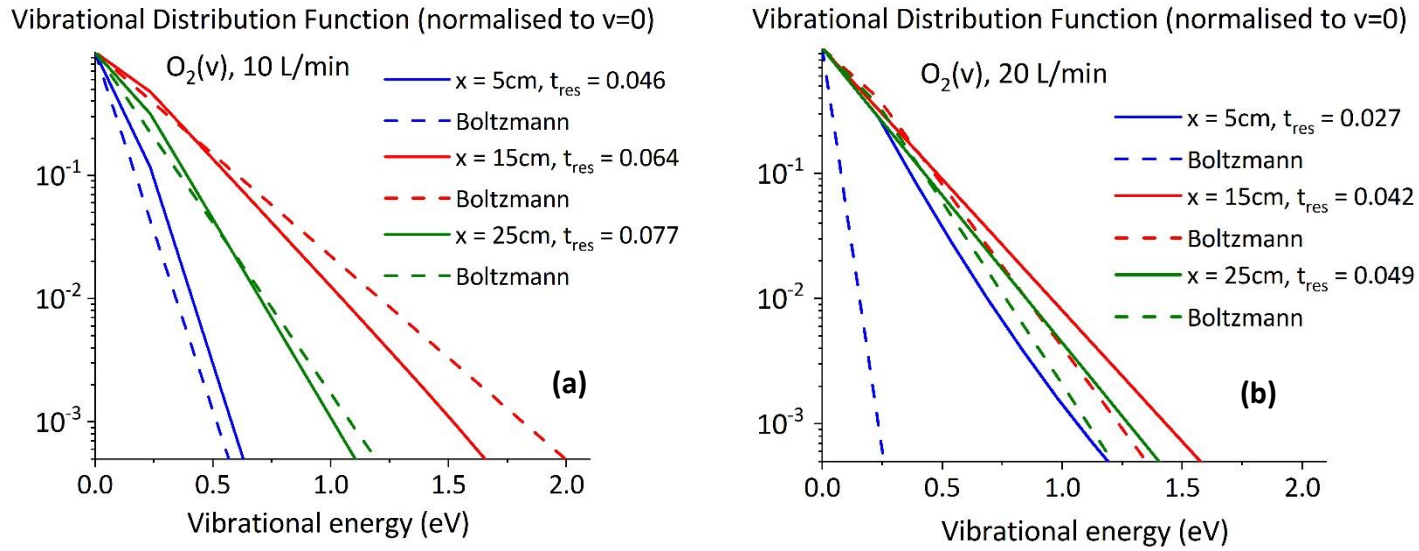

Figure SI.6: *Quasi-1D modelling results of the vibrational distribution of $O_2(v)$ levels for 870 W power,* ***3.5 < r_3 < 8 mm****, at* ***(a)*** *10 L/min and* ***(b)*** *20 L/min. The equivalent Boltzmann distribution is shown along with the VDF at three points inside the plasma region, namely, x=5 cm, x=15 cm and x=25 cm. The residence times up to each point in the discharge are also shown in the accompanying legend.*

References

1. Gordon, I.E., Rothman, L.S., Hill, C., Kochanov, R.V., Tan, Y., Bernath, P.F., Birk, M., Boudon, V., Campargue, A., Chance, K.V., et al. (2017). The HITRAN2016 molecular spectroscopic database. Journal of Quantitative Spectroscopy and Radiative Transfer *203*, 3-69. https://doi.org/10.1016/j.jqsrt.2017.06.038.
2. Emerson Rosemount™ X-STREAM X2GP Continuous Gas Analyzer. https://www.emerson.com/en-us/catalog/rosemount-x-stream-x2gp-continuous-gas-analyzer. (2020).
3. Rueden, C.T., Schindelin, J., Hiner, M.C., DeZonia, B.E., Walter, A.E., Arena, E.T., and Eliceiri, K.W. (2017). ImageJ2: ImageJ for the next generation of scientific image data. BMC bioinformatics *18*, 1-26.
4. Wang, W., Patil, B., Heijkers, S., Hessel, V., and Bogaerts, A. (2017). Nitrogen Fixation by Gliding Arc Plasma: Better Insight by Chemical Kinetics Modelling. ChemSusChem *10*, 2145-2157. 10.1002/cssc.201700095.
5. Vervloessem, E., Aghaei, M., Jardali, F., Hafezkhiabani, N., and Bogaerts, A. (2020). Plasma-Based N2 Fixation into NOx: Insights from Modeling toward Optimum Yields and Energy Costs in a Gliding Arc Plasmatron. ACS Sustainable Chemistry & Engineering *8*, 9711-9720. 10.1021/acssuschemeng.0c01815.
6. Guerra, V., Tejero-del-Caz, A., Pintassilgo, C.D., and Alves, L.L. (2019). Modelling N2–O2 plasmas: volume and surface kinetics. Plasma Sources Science and Technology *28*, 073001. 10.1088/1361-6595/ab252c.
7. Pintassilgo, C.D., and Guerra, V. (2016). Power Transfer to Gas Heating in Pure N2 and in N2–O2 Plasmas. The Journal of Physical Chemistry C *120*, 21184-21201. 10.1021/acs.jpcc.6b05463.
8. Kotov, V., and Koelman, P.M.J. (2019). Plug flow reactor model of the plasma chemical conversion of CO2. Plasma Sources Science and Technology *28*, 095002. 10.1088/1361-6595/ab3774.
9. Hagelaar, G.J.M., and Pitchford, L.C. (2005). Solving the Boltzmann equation to obtain electron transport coefficients and rate coefficients for fluid models. Plasma Sources Science and Technology *14*, 722-733. 10.1088/0963-0252/14/4/011.
10. Van Alphen, S., Vermeiren, V., Butterworth, T., van den Bekerom, D.C.M., van Rooij, G.J., and Bogaerts, A. (2019). Power Pulsing To Maximize Vibrational Excitation Efficiency in N2 Microwave Plasma: A Combined Experimental and Computational Study. The Journal of Physical Chemistry C *124*, 1765-1779. 10.1021/acs.jpcc.9b06053.
11. Kelly, S., Van de Steeg, A., Hughes, A., J. Van Rooij, G., and Bogaerts, A. (2021). Thermal instability and volume contraction in a pulsed microwave N2 plasma at sub-atmospheric pressure. Plasma Sources Science and Technology *0963-0252*. 10.1088/1361-6595.
12. Jardali, F., Van Alphen, S., Creel, J., Ahmadi Eshtehardi, H., Axelsson, M., Ingels, R., Snyders, R., and Bogaerts, A. (2021). NOx production in a rotating gliding arc plasma: potential avenue for sustainable nitrogen fixation. Green Chemistry *23*, 1748-1757. 10.1039/d0gc03521a.
13. Van Alphen, S., Jardali, F., Creel, J., Trenchev, G., Snyders, R., and Bogaerts, A. (2021). Sustainable gas conversion by gliding arc plasmas: a new modelling approach for reactor design improvement. Sustainable Energy & Fuels *5*, 1786-1800. 10.1039/D0SE01782E.
14. Treanor, C.E., Rich, J.W., and Rehm, R.G. (1968). Vibrational Relaxation of Anharmonic Oscillators with Exchange-Dominated Collisions. The Journal of Chemical Physics *48*, 1798-1807. 10.1063/1.1668914.

15. Kelly, S., Golda, J., Turner, M.M., and Schulz-von der Gathen, V. (2015). Gas and heat dynamics of a micro-scaled atmospheric pressure plasma reference jet. Journal of Physics D: Applied Physics *48*, 444002. 10.1088/0022-3727/48/44/444002.
16. Zwolak, J.W., Boggs, P.T., and Watson, L.T. (2007). Algorithm 869: ODRPACK95: A weighted orthogonal distance regression code with bound constraints. ACM Trans. Math. Softw. *33*, 27–es. 10.1145/1268776.1268782.
17. OriginLab Corporation, N., MA, USA. (2018). Origin(Pro), Version Number (e.g. "Version 2018 64-bit"). .